Realistic micromagnetic description of all-optical ultrafast switching processes in ferrimagnetic alloys

V. Raposo,[1,*] F. García-Sánchez,[1] U. Atxitia,[2] and E. Martínez[1,†]
[1]*Departamento de Física Aplicada, Universidad de Salamanca, Salamanca, Spain, 37008*
[2]*Dahlem Center for Complex Quantum Systems and Fachbereich Physik, Freie Universität Berlin, 14195 Berlin, Germany*

(Received 3 December 2021; revised 14 February 2022; accepted 14 March 2022; published 28 March 2022)

Both helicity-independent and helicity-dependent all-optical switching processes driven by single ultrashort laser pulse have been experimentally demonstrated in ferrimagnetic alloys as GdFeCo. Although the switching has been previously reproduced by atomistic simulations, the lack of a robust micromagnetic framework for ferrimagnets limits the predictions to small nanosystems, whereas the experiments are usually performed with lasers and samples of tens of micrometers. Here we develop a micromagnetic model based on the extended Landau-Lifshitz-Bloch equation, which is firstly validated by directly reproducing atomistic results for small samples and uniform laser heating. After that, the model is used to study ultrafast single shot all-optical switching in ferrimagnetic alloys under realistic conditions. We find that the helicity-independent switching under a linearly polarized laser pulse is a pure thermal phenomenon, in which the size of inverted area directly correlates with the maximum electron temperature in the sample. On the other hand, the analysis of the helicity-dependent processes under circular polarized pulses in ferrimagnetic alloys with different composition indicates qualitative differences between the results predicted by the magnetic circular dichroism and the ones from inverse Faraday effect. Based on these predictions, we propose experiments that would allow one to resolve the controversy over the physical phenomenon that underlies these helicity-dependent all optical processes.

DOI: 10.1103/PhysRevB.105.104432

I. INTRODUCTION

All optical switching (AOS) refers to the manipulation of the magnetic state of a sample through the application of short laser pulses. The discovery of subpicosecond demagnetization of a nickel sample [1] upon application of a short laser pulse, ranging from tens of femtosecond to several picoseconds, opened the path for other experiments to manipulate the magnetization using ultrashort laser pulses in ferromagnetic [2,3], synthetic antiferromagnetic [4–6] and ferrimagnetic materials [7–9]. While the AOS in ferromagnetic materials is usually described by the magnetic circular dichroism (MCD) [10,11] or the inverse Faraday effect (IFE) [12–14], and it requires multiple shots of circularly polarized laser pulses [15], the inversion of the magnetization of ferrimagnetic materials can be achieved by a single-shot pulse [16], even with linear polarization. In these helicity-independent AOS (HI-AOS) processes, the reversal takes place as the two antiferromagnetically coupled sublattices demagnetize at different rates when submitted to a laser pulse of adequate duration and energy. Since exchange processes conserve total angular momentum, the system transits through a ferromagnetic-like state despite being ferrimagnetic at the ground state [17]. The switching of the magnetization is completed when the sublattices relax back to their thermodynamic equilibrium [18]. On the other hand, several experimental studies [7,9] have also observed that the magnetic state of ferrimagnetic alloys can be also reversed under circular polarized laser pulses within a narrow range of laser energies, resulting in a helicity-dependent AOS (HD-AOS) which could be useful to develop ultrafast magnetic recording devices purely controlled by optical means. While the single-shot HI-AOS can be caused by the strong nonequilibrium due to the heating induced by the laser pulse, the physical mechanisms behind the HD-AOS are still not completely understood, and several works by the same authors ascribe it either to the IFE [9] or the MCD [8]. Although several attempts have been performed to explain such AOS processes, a realistic numerical description of experimental observations is still missing. Indeed, some theoretical studies usually adopt an atomistic description which is limited to small samples [16,19], with dimensions at the nanoscale, well below the size of the experimentally studied samples, with lateral sizes of several hundreds of microns. Such an atomistic approach cannot describe the nonuniform heating caused by laser beams of several microns, so it does not predict some multidomain patterns typically observed in the experiments [9]. On the other hand, other numerical attempts have been carried out by describing the ferrimagnetic alloy as an effective ferromagnetic sample, without considering the individual nature of the two sublattices forming the ferrimagnet [9]. Although these micromagnetic studies predict some features of the AOS processes, so far, the structure of the ferrimagnetic alloys has not been taken into account to investigate the reversal of magnetic samples of micrometer size under realistic excitation conditions. As the switching happens due to angular momentum transfer between sublattices, something impossible to account for within an effective ferromagnetic

*Corresponding author: victor@usal.es
†Corresponding author: edumartinez@usal.es

description, it is needed to develop studies considering the two sublattice nature of the such alloys to naturally evaluate their role on the reversal processes.

Here we present a micromagnetic framework that is able to reproduce accurately the atomistic results of the laser-induced switching by the extension of the conventional Landau-Lifshitz-Bloch (LLB) model for ferrimagnets [20,21]. Note that the conventional LLB model does not allow us to accurately describe AOS as indicated in Ref. [21], and here we extend it to solve this limitation. However, and differently from atomistic simulations, which are limited to small samples at the nanoscale submitted to uniform laser heating, our micromagnetic formalism allows us to realistically describe AOS experimental observations by directly evaluating extended samples at the microscale and nonuniform energy absorption from the laser pulse. The procedures here developed are essential to understand the physical aspects underlying these experiments, and will be useful for the future development of novel ultrafast devices based on these AOS processes. After presenting and validating both the atomistic and the extended micromagnetic models for sample size of tens of nanometers, the upper size limit of the atomistic spin models, we describe the results for HI-AOS processes in realistic samples at the microscale for a typically ferrimagnetic alloy (GdFeCo). Later on, we focus our attention to the description of the HD-AOS processes by exploring the role of the IFE and MCD separately for two different ferrimagnetic alloys where the relative composition is slightly varied. Our results allow us to suggest future experiments which could be useful to infer the dominance of the IFE or the MCD in single-shot HD-AOS in ferrimagnetic alloys.

II. ATOMISTIC AND MICROMAGNETIC MODELS

Typical ferrimagnetic (FiM) samples formed by a transition metal (TM:Co, CoFe) and a rare earth (RE:Gd) are considered here. Square samples in the xy plane with side length ℓ and with thickness $t_{\mathrm{FiM}} = 5.6$ nm are studied. At atomistic level the FiM sample is formed by a set of coupled spins, and the magnetization dynamics is described the Langevin-Landau-Lifshitz-Gilbert equation

$$\frac{\partial \vec{S}_i}{\partial t} = -\frac{\gamma_0}{(1+\lambda^2)}\{\vec{S}_i \times (\vec{H}_i + \vec{H}_{th,i}) + \lambda \vec{S}_i \times [\vec{S}_i \times (\vec{H}_i + \vec{H}_{th,i})]\}, \quad (1)$$

where $\vec{S}_i$ is the localized magnetic moment and $\vec{H}_i$ is the local effective field including intra- and interlattice exchange and anisotropy contributions. $\vec{H}_{th,i}$ is the local stochastic thermal field. γ_0 and λ are the gyromagnetic ratio and the damping parameter, respectively [22]. Unless otherwise indicated, typical parameters of $\mathrm{Gd}_x(\mathrm{CoFe})_{1-x}$ with relative composition $x = 0.25$ were considered [22]. See Supplemental Material note SN1 [23] for further details, including material and numerical parameters.

Starting from an initial uniform state of the FiM with the spins of the two sublattices antiparallelly aligned each other along the easy axis z, a laser pulse is applied, and the irradiated sample absorbs energy from the laser pulse. The laser spot is assumed to have a spatial Gaussian profile ($\eta(r)$), with r_0 being the radius spot ($d_0 = 2r_0$ is the full width at half maximun, FWHM). Its temporal profile ($\xi(t)$) is also Gaussian, with τ_L representing the pulse duration (FWHM). The absorbed power density can be expressed as $P(r,t) = Q\eta(r)\xi(t)$ where $\eta(r) = \exp[-4\ln(2)r^2/(2r_0)^2]$ is the spatial profile with $r = \sqrt{x^2+y^2}$ being the distance from the center of the laser spot, and $\xi(t) = \exp[-4\ln(2)(t-t_0)^2/\tau_L^2]$ is the temporal profile. Q is the maximum value of the absorbed power density reached at $t = t_0$ just below the center of the laser spot.

Laser pulse heats the FiM sample, and consequently, it is transiently dragged into a nonequilibrium thermodynamic state, where its magnetization changes according to the temperature dynamics. The temperature evolution is described by the two temperatures model (TTM) [9,24] in terms of two subsystems: the electron ($T_e = T_e(\vec{r},t)$) and the lattice ($T_l = T_l(\vec{r},t)$),

$$C_e\frac{\partial T_e}{\partial t} = -k_e\nabla^2 T_e - g_{el}(T_e - T_l) + P(r,t) - C_e\frac{(T_e - T_R)}{\tau_D}, \quad (2)$$

$$C_l\frac{\partial T_l}{\partial t} = -g_{el}(T_l - T_e), \quad (3)$$

where C_e and C_l denote the specific heat of electrons and lattice subsystems, respectively. k_e is the electronic thermal conductivity. g_{el} is a coupling parameter between the electron and lattice subsystems, and τ_D is the characteristic heat diffusion time to the substrate and the surrounding media [25]. Conventional values were adopted (see [1,16,26] and Supplemental Material note SN1 [23]).

The approach that consists on solving Eq. (1) coupled to Eqs. (2) and (3) is named the atomistic spin dynamics (ASD), and due to computational restrictions, its numerical solution is limited to small samples at the nanoscale ($\ell \lesssim 100$ nm, see Supplemental Material note SN2 [23]). While ASD predicts the single-shot switching in small FiM nanosamples [16,22,27], the lack of a realistic micromagnetic framework for microsize samples and nonunifom laser spot limits the description of many experimental works [9]. In particular, the appearance of central regions with a multidomain demagnetized patterns [28], or the observation of rings of switched magnetization under irradiation with lasers of tens of micrometers [29] cannot be reproduced by ASD due to such computing limitations. In order to overcome the ASD limitations, here we develop an extended continuous micromagnetic model that describes the temporal evolution of the reduced local magnetization $\vec{m}_i(\vec{r},t)$ of each sublattice i:RE,TM based on the conventional ferrimagnetic Landau-Lifshitz-Bloch (LLB) Eq [21,30],

$$\frac{\partial \vec{m}_i}{\partial t} = -\gamma'_{0i}(\vec{m}_i \times \vec{H}_i) - \frac{\gamma'_{0i}\alpha_i^{\perp}}{m_i^2}\vec{m}_i \times [\vec{m}_i \times (\vec{H}_i + \vec{\xi}_i^{\perp})] + \frac{\gamma'_{0i}\alpha_i^{\parallel}}{m_i^2}(\vec{m}_i \cdot \vec{H}_i)\vec{m}_i + \vec{\xi}_i^{\parallel}, \quad (4)$$

where $\vec{H}_i = \vec{H}_i(\vec{r},t)$ is the local effective field on sublattice magnetic moment i at location $\vec{r}$ of the FiM sample, $\alpha_i^{\parallel}$ and $\alpha_i^{\perp}$ are the longitudinal and perpendicular damping parameters, and $\vec{\xi}_i^{\parallel}$ and $\vec{\xi}_i^{\perp}$ are the longitudinal and perpendicular

stochastic thermal fields. Details of the LLB model can be found in [21,30] and in Supplemental Material note SN2 [23]. Contrary to the ASD, where the spatial discretization is imposed by the atomistic scale ($a = 0.35$ nm), within the micromagnetic model the sample is discretized in elementary cells with dimensions of $\Delta x = \Delta y \sim 1$nm and $\Delta z = t_{\rm FiM}$. Therefore, it is possible to numerically evaluate, with manageable computing effort, extended samples at the microscale ($\ell \sim 100\ \mu$m), three orders of magnitude larger than the ones which can be dealt with the ASD model.

Numerically solving Eq. (4) coupled to Eqs. (2) and (3) under ultrashort laser pulses provides a micromagnetic description of several AOS processes in ferromagnetic systems [13]. However, when dealing with ferrimagnetic samples we checked that some disagreement with the predictions of the ASD model were observed (see Supplemental Material note SN3 [23]), which are related to the lack of a proper description of the angular moment exchange between sublattices during the nonequilibrium transient state promoted by the laser pulse. Indeed, magnetization dynamics in FiMs is driven by dissipative processes of relativistic and exchange nature. The relativistic ones allow exchange of angular momentum between the magnetization and the lattice degrees of freedom due to the spin-orbit coupling between them, and are phenomenologically described by the usual damping terms in the LLB Eq. (4). Additionally, in multisublattice magnets as FiMs, another different pathway opens local exchange of angular momentum between both sublattices of the FiM, and to account for it, the LLB Eq. (4) has to be enhanced by an additional exchange relaxation torque [18,31–34]. The simplest model to describe the sublattice-specific magnetization dynamics in FiMs, was derived from Onsager's relations [31] within a macrospin approach based on a microscopic spin model. In this simplified description, the magnetization dynamics of sublattice i can be expressed as $\frac{1}{\gamma_{0i}}\frac{dm_i}{dt} = \alpha_i H_i + \alpha_{\rm ex}(\frac{\mu_i}{\mu_j}H_i - H_j)$, where i, j : RE, TM, μ_i and H_i are the magnitude of the magnetic moment and the effective field acting on macrospin of sublattice i, respectively. The relativistic relaxation parameter in this model, α_i, corresponds to the longitudinal damping parameter in the LLB equation and it depends on the temperature of the thermal bath to which angular momentum and energy is dissipated. In contrast, it is assumed that the exchange relaxation parameter $\alpha_{\rm ex}$, only depends on the nonequilibrium sublattice magnetizations, $\alpha_{\rm ex} = \alpha_{\rm ex}(m_i, m_j)$. Considering that the exchange relation rate should be symmetric with respect to the sublattice index, $\alpha_{\rm ex}(m_i, m_j) = \alpha_{\rm ex}(m_j, m_i)$, a simple functional fulfilling these heuristic conditions yields $\alpha_{\rm ex}(m_i, m_j) = \lambda_{\rm ex}\frac{m_i + (x_j\mu_j/x_i\mu_i)m_j}{m_i m_j}$ where $\lambda_{\rm ex}$ is a phenomenological parameter representing the exchange relaxation rate and x_i the concentration of each specimen i. Inspired by this two sublattice phenomenological model based on Onsager's relations, here we add an additional torque $\vec{\tau}_i^{\rm NE}$ to the micromagnetic LLB Eq. (4) that accounts for nonequilibrium magnetic moment exchange between sublattices, and becomes crucial to describe AOS ultrafast switching in FiMs under realistic conditions. The torque reads as

$$\vec{\tau}_i^{\rm NE} = \gamma'_{0i}\lambda_{\rm ex}\alpha_i^{\parallel}\frac{x_i\mu_i m_i + x_j\mu_j m_j}{\mu_i m_i \mu_j m_j}(\mu_i\vec{H}_i^{\parallel} - \mu_j\vec{H}_j^{\parallel}), \qquad (5)$$

where and $\vec{H}_i^{\parallel}$ and $\vec{H}_j^{\parallel}$ are the longitudinal effective fields for each lattice i:RE,TM [21], $x_i \equiv x$ and $x_j = 1 - x_i = 1 - x$ are the concentrations of each specimen, and $\lambda_{\rm ex}$ is a parameter representing the exchange relaxation rate [18]. By including Eq. (5) in the RHS of Eq. (4), and numerically solving it coupled to TTM Eqs. (2) and (3), we can provide a realistic description of the magnetization dynamics in FiM systems under ultrashort laser pulses. In what follows, we refer to this formalism as the extended micromagnetic LLB model (eLLB), to distinguish it from the conventional LLB model (LLB) when $\vec{\tau}_i^{\rm NE} = 0$. See Supplemental Material note SN2 [23] for the rest of details.

III. RESULTS AND DISCUSSION

Before presenting the predictions of the extended micromagnetic model for realistic FiM samples and laser beams at the microscale, here we firstly compare the results obtained from the extended LLB model (eLLB) to the ones resulting from the atomistic spin dynamics simulations (ASD) for a small FiM dot at the nanoscale ($\ell \approx 25$ nm). As typical laser spots have radius of $r_0 \sim 1\ \mu$m $- 10\ \mu$m or even larger, we assume here that the power absorbed by the FiM dot the from the laser pulse is uniform, that is, $\eta(r) = 1$. The pulse duration is $\tau_L = 50$ fs. Typical results showing the temporal evolution of the out-of-plane averaged magnetization (m_z^i) for each sublattice [i : TM (red), RE (blue)] are shown in Fig. 1 for two different values of Q.

A remarkable agreement between both ASD and eLLB models with similar dynamics for both sublattices is observed in Figs. 1(a) and 1(b). For low Q values [Fig. 1(a) and 1(c)] there is no switching, but when Q increases above a threshold, which depends on the pulse length (τ_L), the deterministic AOS is predicted by both ASD and eLLB models [Figs.1(b) and 1(e)]. It is important to note that similar switching was also obtained within the deterministic eLLB framework, that is, in the absence of thermal fluctuations ($\vec{\xi}_i^{\perp} = \vec{\xi}_i^{\parallel} = 0$ in Eq. (4), see Fig. S4(b) in Supplemental Material Note SN3 [23]). On the contrary, the conventional LLB model (LLB, $\vec{\tau}_i^{\rm NE} = 0$) fails to reproduce the switching of Fig. 1(b) [see Figs. S4(c)–S4(d) in Supplemental Note SN3 [23]). Figure 1(c) shows the details of the temporal evolution m_z^i for $Q = 6 \times 10^{21}$ W/m^3 during the first laser pulse, while the corresponding evolutions of T_e and T_l are depicted in Fig. 1(d), which also shows the laser pulse. Corresponding results for $Q = 12 \times 10^{21}$ W/m^3 are shown in Figs. 1(e) and 1(f), respectively. For $Q = 6 \times 10^{21}$ W/m^3, the electron temperature reaches a peak maximum value of $T_e \approx 850$ K at the end of the laser pulse, but this is not enough to achieve the switching. For $Q = 12 \times 10^{21}$ W/m^3, T_e reaches a peak of $T_e \approx 1150$ K and switching takes place. Notice that this value is well above the Curie temperature ($T_C \approx 600$ K), and therefore the system needs to be significantly heated above the Curie threshold to achieve the deterministic AOS in FiM. These processes are explained by the different demagnetization rates of the RE and TM sublattices, that lead to a transient ferromagnetic aligment. Such a transient ferromagnetic state is observed during a short transient [see shaded interval in Fig.1(e)], and it is only present when the system is far away from the thermodynamic

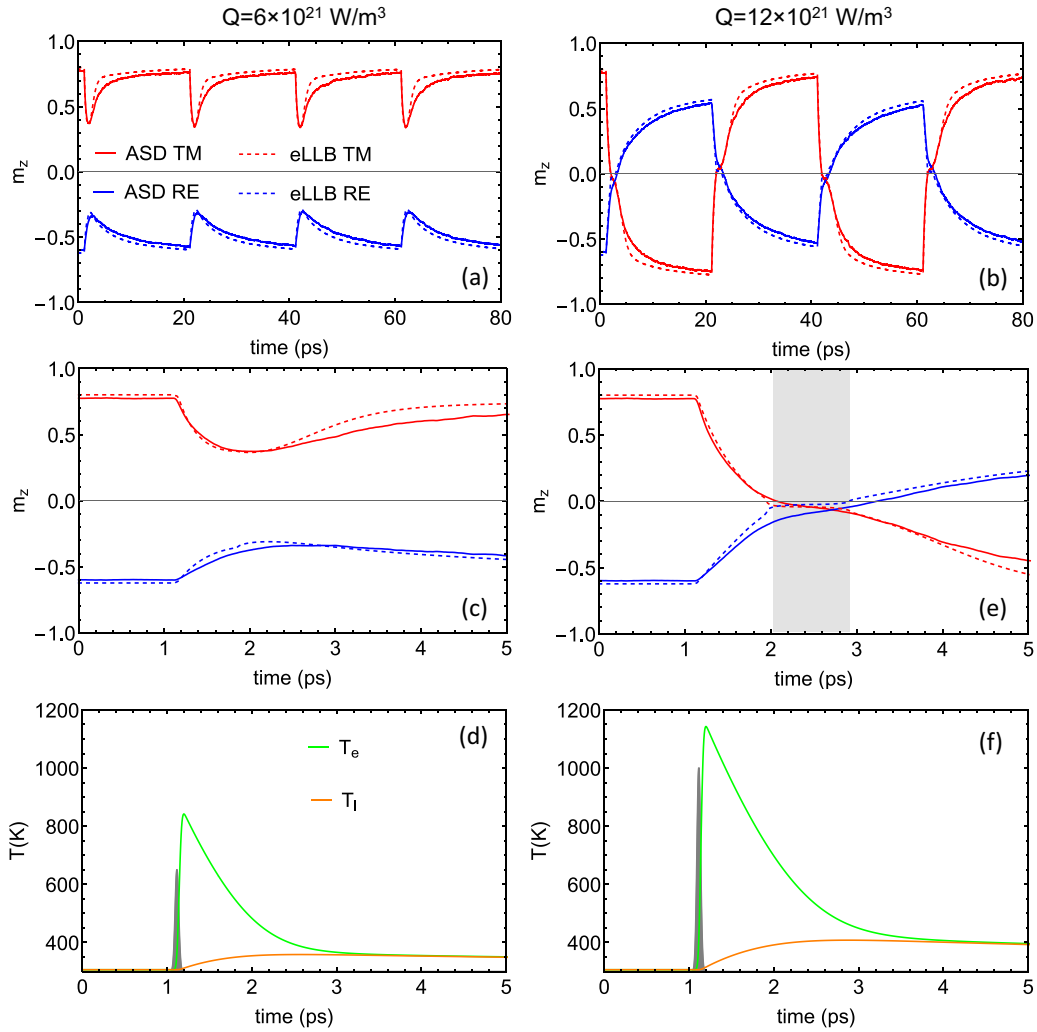

FIG. 1. Comparison between atomistic simulation (ASD, solid lines) and micromagnetic model (eLLB, dashed lines) results for the temporal evolution of the out-of-plane magnetization for the transition metal (TM, red) and the rare earth (RE, blue) under two different laser power densities: (a) $Q = 6 \times 10^{21}$ W/m^3 and (b) $Q = 12 \times 10^{21}$ W/m^3. Four consecutive laser pulses with $\tau_L = 50$ fs are applied every 20 ps. (c) shows a detailed view of first pulse switching event as in (a), while (d) shows temporal evolution of the electron (T_e) and lattice (T_l) temperatures for $Q = 6 \times 10^{21}$ W/m^3. (e) and (f) corresponds to $Q = 12 \times 10^{21}$ W/m^3. Shaded interval in (e) shows the transient ferromagnetic state. The pulse length is $\tau_L = 50$ fs. The eLLB results were obtained with $\lambda_{ex} = 0.013$.

equilibrium, as caused by the ultrafast laser heating. Except the contrary is indicated, all eLLB results were obtained with $\lambda_{ex} = 0.013$, (see Fig. S5 and its corresponding discussion in Supplemental Material Note SN3(c) [23] for results with other values of λ_{ex}).

Helicity-independent all optical switching (HI-AOS). Once validated the eLLB formalism by reproducing the ASD results for small nanosamples under uniform linearly polarized laser pulses, we can now use it to explore the influence of the laser duration (τ_L) and maximum absorbed power density (Q) in realistic extended samples at the microscale ($\ell \sim 10$ μm). This is illustrated in the phase diagram of Fig. 2(a), which shows the final state under a single linearly polarized laser pulse starting from a uniform state of the FiM. White color indicates the combinations of (Q, τ_L) where the sample returns to the original state after the pulse (no-switching). The blue region corresponds to combinations of (Q, τ_L) presenting deterministic HI-AOS after each pulse, and red corresponds to combinations of (Q, τ_L) resulting in a final demagnetized multidomain configuration. It is noted that there is a correlation between the final state and the maximum electron temperature reached in the sample, which is shown by the overlapping solid black lines in Fig. 2(a). As it is clearly observed, solid lines coincide with boundaries between the three possible behaviors already discussed. Indeed, the transition between no-switching (white) to the deterministic switching range (red) is limited by the ~ 1000 K curve, whereas the transition to the thermal demagnetization (blue) occurs when $T_e \gtrsim 1400$ K, as shown in Fig. 2(a). Instead of Q, the information collected in the phase diagram of Fig. 2(a) could be also presented in terms of the laser fluence ($F \equiv Q\, \tau_L\, t_{\mathrm{FiM}}$), as it is done in Fig. S6 of Supplemental Material note SN4 [23]. Note that such phase diagram is also in good qualitative agreement with recent experimental observations [35].

The main advantage of the extended eLLB model over ASD simulations is that it allows us to explore realistic

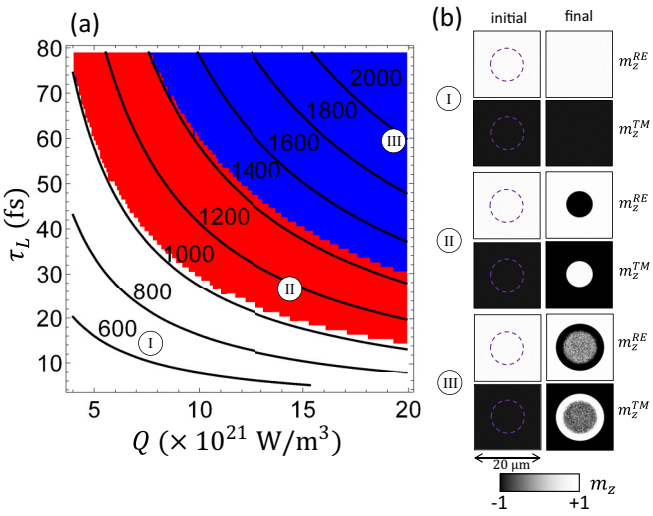

FIG. 2. (a) Phase diagram of the final state as a function of Q and τ_L for a small nanosample $\ell = 25$ nm under uniform laser heating ($\eta(r) = 1$). White, red and blue colors represent no-switching, deterministic switching, and thermal demagnetization behaviors, respectively. Solid lines are isothermal curves showing the maximum electron temperature (T_e) reached due to the pulse. (b) Typical micromagnetic snapshots of the initial and final magnetization of RE and TM for three combinations of (Q, τ_L). I: (8×10^{21} W/m^3, 20 fs), II: (15×10^{21} W/m^3, 30 fs) and III: (20×10^{21} W/m^3, 60 fs). Here extended samples ($\ell = 20$ μm) with a laser spot of $d_0 = \ell/2$ were considered. Dashed purple lines in the images of the initial state indicate the FWHM of the laser spot. The results of the phase diagram (a) coincide with (b) for magnetization at the center of the laser spot.

samples and laser beams with dimensions that are not accessible with ASD models. eLLB model [Eqs. (4) and (2)–(3)] has been used to simulate samples with lateral size of $\ell = 20$ μm. From now on, the spatial Gaussian dependence of the laser beam is considered ($\eta(r) = \exp[-4\ln(2)r^2/(2r_0)^2]$), with a laser spot diameter of $d_0 = 2r_0 = \ell/2$. Typical initial and final states corresponding to three representative combinations of (Q, τ_L) are shown in Fig. 2(b). Our micromagnetic simulations point out again that the three types of behaviors observed experimentally (see for example Fig. 4(a) in Refs. [9] or [6,28]) are also achieved under these realistic conditions, with samples and laser spots at the microscale. Notice that now the final magnetic state depends on the local position because the power absorption from laser pulse does. The final states depict a radial symmetry around the center of the laser spot, which coincides with the center of the FiM sample at $(x_c, y_c) = (0, 0)$.

In order to further describe such spatial dependence, Fig. 3 plots the final state of m_z^{TM} as a function of x along the central line of the FiM sample ($y = 0$) for the same three representative combinations of (Q, τ_L) as in Fig. 2(b). The maximum electron temperature $T_e = T_e(x)$ is also plotted in top graphs by blue curves. The bottom graphs in Fig. 3 show the final state over the sample plane (x, y). These graphs clearly correlate the local final magnetic state ($m_z^{\mathrm{TM}}(x, y)$) with the maximum electron temperature $T_e(x, y)$. In the no-switching regime (I), the electron temperature does not reach 1000 K at any point. For combinations (Q, τ_L) as II, $T_e(x) \gtrsim 1000$ K is only reached in the central region, whose dimensions fit the local part of the sample that switches its magnetization. Note that T_e remains below $T_e(x) \lesssim 1400$ K. Finally, the demagne-

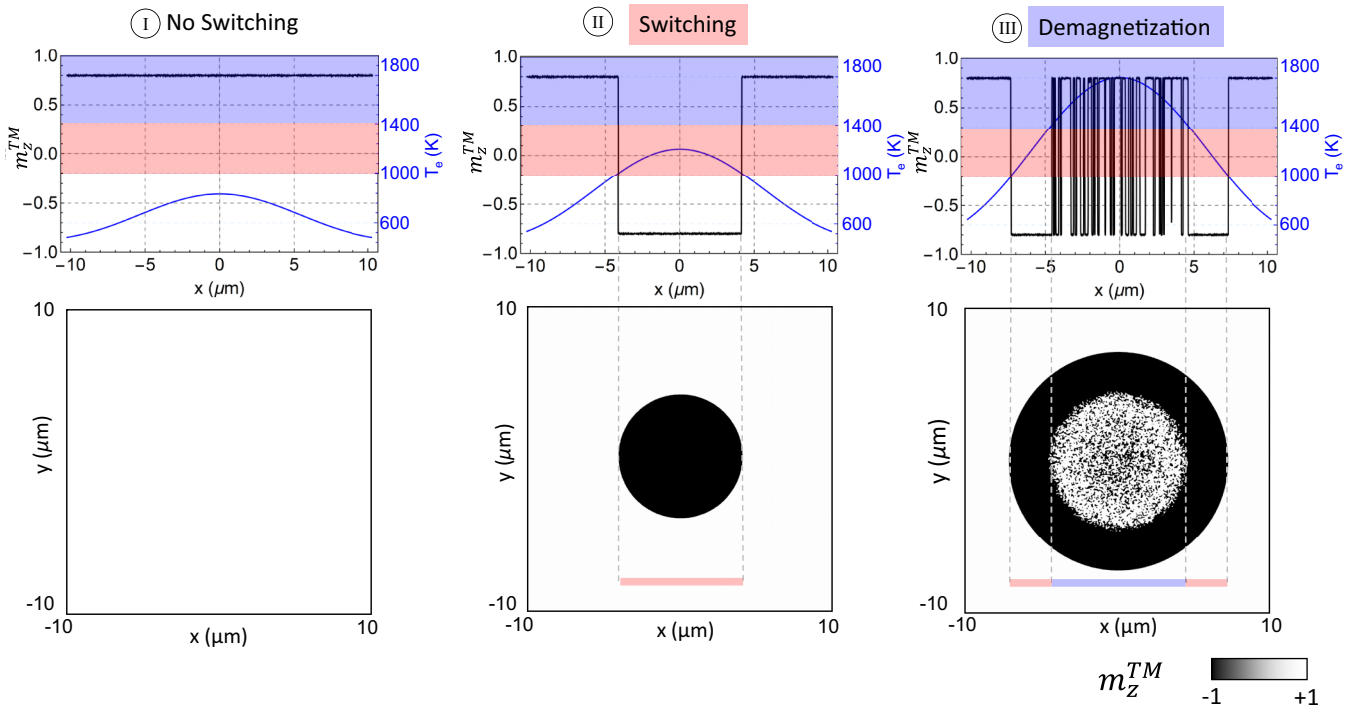

FIG. 3. Final out-of-plane magnetization ($m_z^{\mathrm{TM}}(x)$) and maximum electron temperature ($T_e(x)$) as function of x for $y = 0$ and for the three representative combinations of (Q, τ_L) as in Fig. 2(b) (top graphs). The corresponding final states over the sample plane (x, y) are shown in bottom graphs.

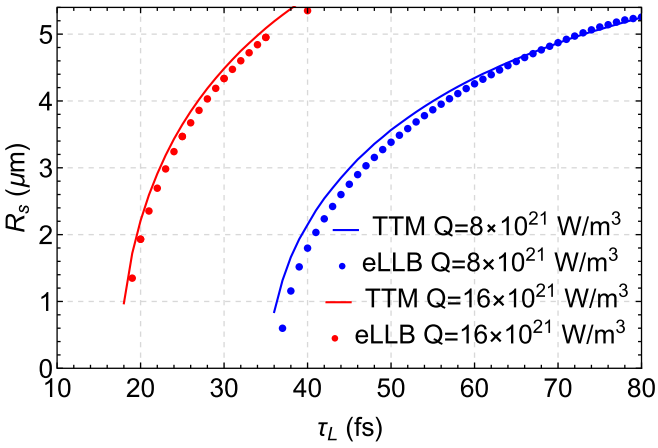

FIG. 4. Radius of the switched area (R_s) as a function of laser duration (τ_L) for two values of the maximum absorbed power (Q). Dots are micromagnetic results from the extended eLLB model. Lines are predictions from the TTM, where R_s is inferred from the condition that the local maximum electron temperature reaches $T_e \gtrsim 1000$ K.

tized case (multidomain pattern, III) occurs in the part of the sample where $T_e \gtrsim 1400$ K, but deterministic switching is still obtained in the ring region, where $1000\ \text{K} \lesssim T_e(x) \lesssim 1400$ K. Micromagnetic images (bottom graphs in Fig. 3) are in good agreement with typical experimental HI-AOS observations [6,28].

The inferred correlation between the maximum electron temperature and the final magnetic state allows us to predict the size of the inverted region by studying the maximum electron temperature reached in the sample by using the TTM [Eqs. (2) and (3)] in combination with the switching diagram of Fig. 2(a). The radius of the switched area (R_s) calculated from micromagnetic simulations (dots, eLLB), and the one predicted by the TTM (lines, TTM) is shown in Fig. 4 as function of τ_L for two different values of Q within the deterministic switching range ($1000\ \text{K} \lesssim T_e(x) \lesssim 1400$ K). Again, good agreement is obtained, a fact that points out that the origin of these HI-AOS processes under linearly polarized laser pulse is a purely thermal phenomenon. Indeed, as the local maximum electron temperature reached in the sample only depends on the absorbed power from the laser (Q) and the laser pulse length (τ_L), the size of the inverted region can be directly obtained from the TTM by the condition of $T_e \gtrsim 1000$ K.

Helicity-dependent all optical switching (HD-AOS). Previous results were carried out by applying laser pulses with linear polarization ($\sigma = 0$), and show that the HI-AOS can be achieved in a controlled manner with an adequate election of the laser power (Q) and duration (τ_L): the magnetization switches its direction in the picoseconds range independently on the initial state. While this is interesting for toogle memory applications, the procedure to store and record a bit using linearly polarized laser pulses would still require two steps: (i) a preliminary reading operation of the magnetic state, and after that (ii) deciding or not to apply the laser pulse depending on the preceeding state. This two-step procedure can be avoided by using circularly polarized laser pulses, resulting in HD-AOS. However, as it was already commented the physics behind these HD-AOS observations still remains unclear, and both the MCD [8,10] and the IFE [12,14] have been suggested as responsible of the experimental observations. In what follows, we explore both mechanisms in a separated manner by including them in the extended micromagnetic model.

Let us firstly consider MCD. It has been suggested to be play a dominant a role on these HD-AOS processes in GdFeCo ferrimagnetic samples, which are known for its strong magneto-optical effect [8]. According to the MDC formalism, right-handed (σ^+) and left-handed (σ^-) circularly polarized laser pulses experience different refractive indices, and consequently a difference in energy absorption of the FiM sample for σ^+ and σ^- pulses is expected. The MCD coefficient can be calculated from the total absorption for each polarization, resulting in $\text{MCD} \equiv k = (A_- - A_+)/(\frac{1}{2}(A_+ + A_-))$, where $A_\pm$ represent the total absorption for each polarization, ($\pm \equiv \sigma^\pm$). Indeed, the MCD makes the power absorbed by the sample ($P(r,t)$) to depend on the laser helicity ($\sigma^\pm = \pm 1$ for right-handed and left-handed circular helicities) and on the initial net magnetic state ($m_N(0) = M_S^{\text{TM}} m_z^{\text{TM}}(0) + M_s^{\text{RE}} m_z^{\text{RE}}(0)$), *up* ($\uparrow$: $m_N(0) > 0$) or *down* ($\downarrow$: $m_N(0) < 0$). Note that $m_z^{\text{TM}}(0) = \pm 1$ and $m_z^{\text{RE}}(0) = \mp 1$, whereas M_S^{TM} and M_S^{RE} are both positive. Under a right-handed laser pulse (σ^+), an initially *up* (*down*) magnetic state is expected to absorb more (less) energy than the initially *down* (*up*) state. Therefore, $P(r,t)$ in Eq. (2) is replaced by $\psi(\sigma^\pm, m_N)P(r,t)$ with $\psi(\sigma^\pm, m_N) = (1 + \frac{1}{2}k\sigma^\pm \text{sign}(m_N))$ describing the different absorption power for *up* and *down* magnetization states as depending on the laser helicity. See further details on the implementation of the MCD in Supplemental Material note SN5 [23].

We have evaluated the role of the MCD in the eLLB model with several values of the MCD coefficient (k). The isothermal curve delimiting the border between the no-switching and switching regimes now depends on the combination of helicity and initial net magnetic state (see such isothermal threshold curves for different values of the MCD coefficient in of SN5). Considering a realistic value of $\text{MCD} \equiv k \sim 2\%$, as estimated in Ref. [8], the electron temperature variation is quite small, typically a few units of K, and therefore small variations in the phase diagram are obtained with respect to the one for linearly polarized pulses Fig. 2(a) (see also Fig. S7 in Supplemental Material note SN5 [23]). However, when exciting with circular polarized pulses close to the no-switching/switching boundary, the FiM switches or not depending on the helicity and initial net state, only within a narrow interval of Q. This is represented in Fig. 5(a), where the HD-AOS is shown for $\tau_L = 50$ fs pulses with different Q in a sample with $\ell = 20$ μm. Note that these results correspond to a FiM alloy $\text{Gd}_x(\text{FeCo})_{1-x}$ with $x = 0.25$, and that for this relative composition the RE is the dominant sublattice at room temperature, $M_s^{\text{RE}} > M_s^{\text{TM}}$ at $T = 300$ K (see inset of Fig. S3 of the Supplemental Material [23] or Fig. 6(a)). No switching is achieved for low energy values [see left column in Fig. 5(a) for $Q = 5.7 \times 10^{21}$ W/m^3]. However, if Q increases to $Q = 5.8 \times 10^{21}$ W/m^3, the system shows the so-called HD-AOS: if m_z^{RE} is initially *down* (*up*), the reversal is only achieved for left-handed helicity, $\sigma^- = -1$ (right-handed helicity, $\sigma^+ = +1$). Consequently, the final state can be selected by chosing the laser helicity, which is relevant for ultrafast memory applications. It is important to note that this helicity dependent

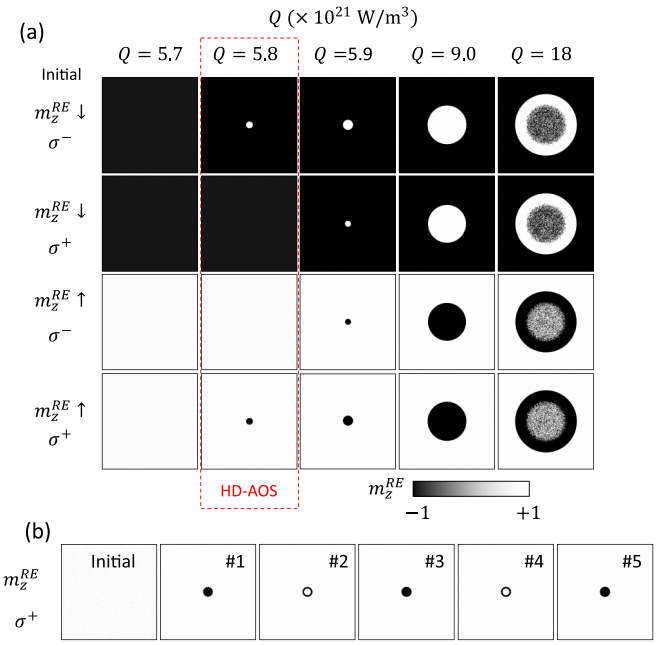

FIG. 5. Helicity-dependent AOS predicted by the MCD. (a) Snapshots of the final RE magnetic state (m_z^{RE}) after a laser pulse of $\tau_L = 50$ fs for five different values of the absorbed power density (Q). Results are shown for four combinations of the initial state (↑, ↓) and helicities ($\sigma^{\pm}$) as indicated at the left side. The HD-AOS is shown in panel corresponding to $Q = 5.8 \times 10^{21}$ W/m^3. (b) RE magnetic state after every pulse for $Q = 5.9 \times 10^{21}$ W/m^3, showing the appearance of a ring due to the MCD and the switching of the central part. Here pulses with left-handed chirality are applied (σ^+). The sample side is $\ell = 20$ μm and the laser spot diameter is $d_0 = \ell/2$.

AOS is only obtained in a very narrow range of Q around the helicity independent AOS boundary. Indeed, a small increase of the absorbed power results again in HI-AOS as the linear polarized case (see third and fourth columns in Fig. 5(a) for $Q = 5.9 \times 10^{21}$ W/m^3 and $Q = 9.0 \times 10^{21}$ W/m^3). For high values of Q, the final state depicts a ring around a central demagnetized state, similar to the HI-AOS case [see right column in Fig. 5(a) for $Q = 18 \times 10^{21}$ W/m^3]. In this case, the maximum electron temperature overcomes the $T_e \simeq 1400$ K threshold in the central region below the laser spot, resulting in a central demagnetized or multidomain state. However, the maximum T_e remains within the range of HD-AOS deterministic switching [1000 K $\lesssim T_e(x) \lesssim$ 1400 K] in the ring around the central part. These micromagnetic predictions, including the narrow range of HD-AOS, are in good agreement with several experimental observations (see, for instance, Fig. 4 and 7(a) in Ref. [9], Fig. 1(b) in Ref. [4], or Fig. 3 in Ref. [36]).

Moreover, the inclusion of the MCD in our eLLB model allows us to explain the experimental observation of rings [28,36,37] which appear after the application of a second laser pulse. This is illustrated in Fig. 5(b) for pulses with $Q = 5.9 \times 10^{21}$ W/m^3 and $\tau_L = 50$ fs. The central part of the sample reaches temperatures that lead to HI-AOS, and therefore, its magnetization reverses after each pulse. On the contrary, the ring around of the inverted region is within the HD-AOS regime, and therefore, its local magnetic state (going from *up* to *down*) is only reversed by the first pulse. For the second and subsequent pulses, the ring maintains its *down* state while the inner part changes again to *up* (white). This is repeated every pulse, with the inversion of the central part and the maintenance of black ring in the external shell, as it is clearly seen in even pulses [see snapshots after pulses #2 and #4 in Fig. 5(b)]. Note that this ring structure differs from the ones shown in Fig. 2(b) and Fig. 3, as they were caused by the inversion of the magnetization around the central demagnetized part under high-power linear pulses ($\sigma = 0$). For circularly polarized pulses ($\sigma^{\pm} = \pm 1$) the images correspond to alternative switching and the HD-AOS without the central demagnetized (multidomain) state. Again, these results are in good agreement with recent experimental observations (see figures in Refs. [28,36,37]).

Instead of the MCD, several other works claim that the observations of the HD-AOS can be ascribed to the IFE [9]. Within this formalism, the laser pulse generates an effective out-of-plane magneto-optical field which direction depends on the laser pulse helicity, $\vec{B}_{\mathrm{MO}}(\vec{r},\, t) = \sigma^{\pm} B_{\mathrm{MO}} \eta(r) \epsilon(t) \vec{u}_z$, where $\eta(r) = \exp[-4\ln(2) r^2 / (2r_0)^2]$ is the spatial field profile, and $\epsilon(t)$ is its temporal profile. Note that the spatial dependence of $\vec{B}_{\mathrm{MO}}(\vec{r},\, t)$ is the same as the one of the absorbed power density. However, according to the literature [9], the so-called magneto-optical field $\vec{B}_{\mathrm{MO}}(\vec{r},\, t)$ has some temporal persistence with respect to the laser pulse, and therefore its temporal profile is different for $t < t_0$ and $t > t_0$: $\epsilon(t < t_0) = \exp[-4\ln(2)(t - t_0)^2 / \tau_L^2]$, and $\epsilon(t \geqslant t_0) = \exp[-4\ln(2)(t - t_0)^2 / (\tau_L + \tau_D)^2]$, where τ_D is the delay time of the $\vec{B}_{\mathrm{MO}}(\vec{r},\, t)$ with respect to the laser pulse. We have evaluated this IFE scenario by including this field $\vec{B}_{\mathrm{MO}}(\vec{r},\, t)$ in the effective field of Eq. (4). The results for the same FiM alloy considered up to here $(\mathrm{Gd}_x(\mathrm{FeCo})_{1-x}$, with $x = 0.25$, see SN5), are similar to the ones already presented in Fig. 5 for the MCD considering a maximum magneto-optical field of $B_{\mathrm{MO}} = 20$ T with a delay time of $\tau_D = \tau_L$. These IFE results can be seen in Fig. S8 in Supplemental Material Note SN6 [23]. Therefore, we could conclude from this analysis that, from the micromagnetic modeling point of view, both the MCD and the IFE are compatible with experimental observations of the HD-AOS. At this point, it is worth mentioning here that in real experiments there is not a clear distinction between MCD and IFE phenomena. Indeed, the modeling of the IFE for absorbing materials can account for absorption phenomena as MCD (see for instance [38,39]). These works suggested that in micromagnetic simulations the IFE could induce a change of the magnetic moment ($\Delta\vec{m}_i$) modifying the initial magnetic moments in the two sublattices of the FiM when submitted to circular polarized laser pulses. We have evaluated in our modeling this alternative manner of studying the role of the IFE by adding such an induced magnetic moment in the eLLB Eq. (4), and compared the results to the case where the IFE is simulated by the magneto-optical field $\vec{B}_{\mathrm{MO}}(\vec{r},\, t)$ as discussed above. As presented and discussed in Supplemental Material note SN7 [23], both alternatives ($\vec{B}_{\mathrm{MO}}(\vec{r},\, t)$ or $\Delta\vec{m}_i$) are equivalent from the simulation point of view. Therefore, in what follows we will simulate the IFE as an effective out-of-plane magneto-optical field.

In order to get a further understanding on the physics of these two mechanisms, either the MCD or the IFE, we have

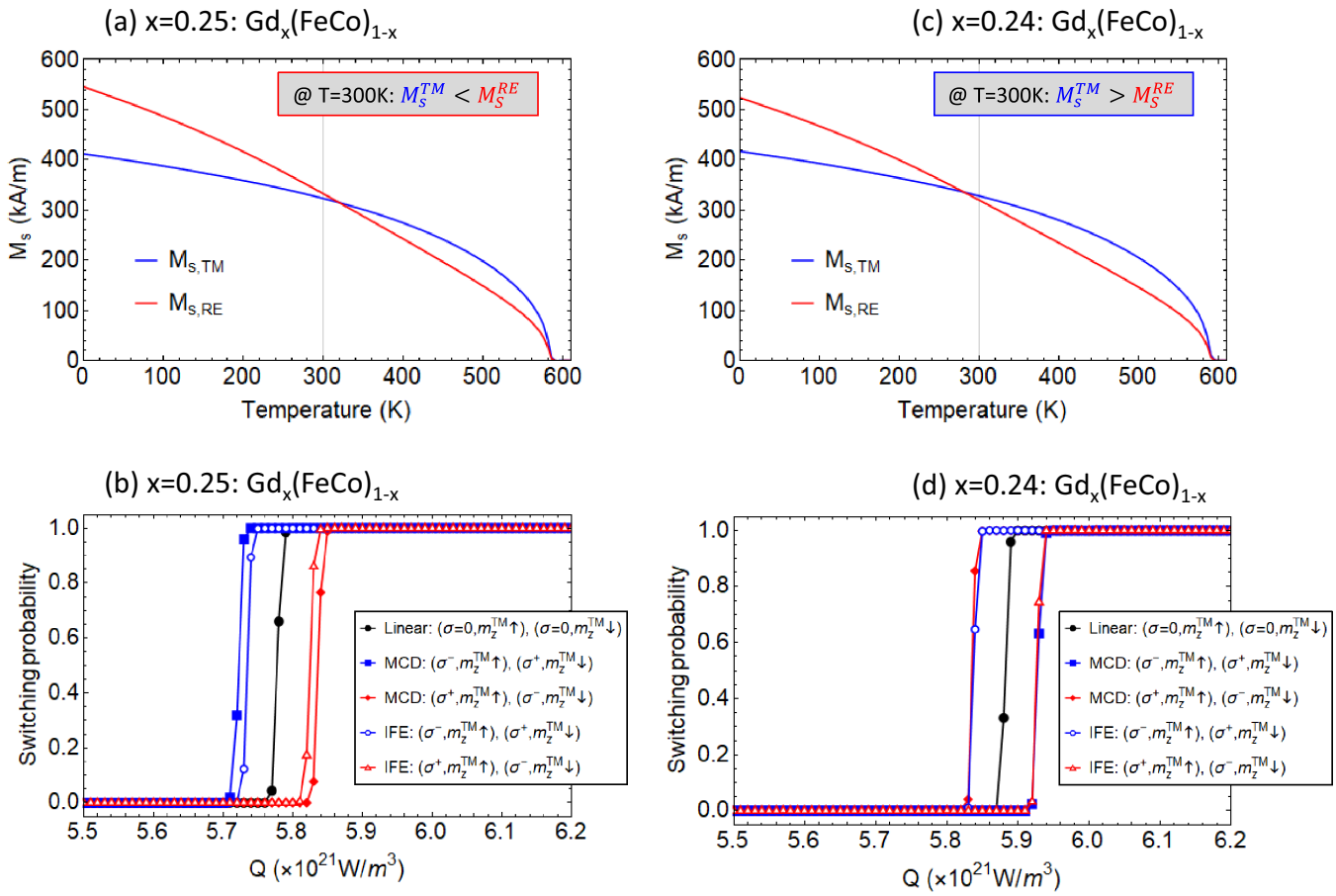

FIG. 6. Temperature dependence of the spontaneous magnetization of each sublattice (RE:Gd; TM:CoFe) of the FiM alloy $(Gd_x(CoFe)_{1-x}$ for two different compositions: (a) $x = 0.25$ and (c) $x = 0.24$. The vertical grey line indicates the initial room temperature prior the laser pulse ($T = 300$ K). Probability of switching as a function of the absorbed power density (Q) for a laser pulse of $\tau_L = 50$ fs for different combinations of the initial state ($m_z^{\mathrm{TM}} : (\uparrow, \downarrow)$) and the polarization (linear: $\sigma = 0$ (black dots), and circular $\sigma^{\pm} = \pm 1$) of the laser pulse as indicated in the legend and in the main text: (b) corresponds to $x = 0.25$ and (d) to $x = 0.24$. MCD results are shown by solid dots, whereas IFE results are presented by open symbols. Lines are a guide to the eyes.

explored the switching probability as a function of Q for laser pulses with fixed duration ($\tau_L = 50$ fs) in two FiM alloys with slightly different composition: $Gd_x(FeCo)_{1-x}$ with $x = 0.25$ and $x = 0.24$ respectively. The corresponding parameters to numerically evaluate these two alloys are given in SN8, and the temperature dependence of the saturation magnetization of each sublattice (RE: Gd; TM: CoFe) are shown in Figs. 6(a) and 6(c), respectively. Note that magnetization compensation temperature at which the net magnetization of the sample vanishes (T_M) is above and below room temperature for $x = 0.25$ and $x = 0.24$ respectively. In other words, the FiM sample is dominated by the RE (TM) at $T = 300$ K for $x = 0.25$ ($x = 0.24$) compositions. The MCD and IFE parameters remain fixed as indicated above (MCD: $k \sim 2\%$,; IFE: $B_{\mathrm{MO}} = 20$ T, $\tau_D = \tau_L$). The two possible initial states prior to the laser pulse ($m_z^{\mathrm{TM}} : (\uparrow, \downarrow)$), and the three laser polarizations (linear: $\sigma = 0$, and circular $\sigma^{\pm} = \pm 1$) were evaluated. The switching probability was computed by evaluating ten different stochastic realizations for each for each Q, and the results are presented in Figs. 6(b) and 6(d) for $x = 0.25$ and $x = 0.24$ respectively. As in experimental observations [9], the HD-AOS takes place only in a narrow range of Q around the threshold value of Q at which the switching probability abruptly changes from 0 to 1 under linear polarized pulses [black dots in Fig. 6(b) and 6(d)].

For $x = 0.25$, as all results presented up to here, the FiM is dominated by the RE:Gd at room temperature: $M_s^{\mathrm{TM}} < M_s^{\mathrm{RE}}$ at $T = 300$ K, see Fig. 6(a). In this case, the switching requires less Q with circular polarization ($\sigma^{\pm}$) with respect to the linearly polarized case ($\sigma = 0$) for two different combinations of the circular laser polarization and the initial state of the FiM: (σ^-, $m_z^{\mathrm{TM}} \uparrow$) and ($\sigma^+$, $m_z^{\mathrm{TM}} \downarrow$). This happens for both MCD (solid symbols) and IFE scenarios (open symbols) as it is shown in Fig. 6(b). Note that the initial state in the TM is the opposite to the RE: $m_z^{\mathrm{TM}} \uparrow$ (*up*) corresponds to $m_z^{\mathrm{RE}} \downarrow$ (*down*) and vice, and the AOS is independent on the initial state for linear polarization (HI-AOS), whereas under circular polarized laser pulses the switching is HD-AOS. For the rest of combinations, either (σ^+, $m_z^{\mathrm{TM}} \uparrow$) or ($\sigma^-$, $m_z^{\mathrm{TM}} \downarrow$), a higher Q is needed to achieve 100% of switching probability with respect to the linear polarized laser pulse, and again for $x = 0.25$ both MCD and IFE scenarios result in similar behavior of the switching probability [Fig. 6(b)].

Remarkably, the MCD and IFE results are qualitatively different when the composition is slightly modified to $x = 0.24$,

where the FiM becomes dominated by the TM:CoFe at room temperature: $M_s^{\mathrm{TM}} > M_s^{\mathrm{RE}}$ at $T = 300$ K, see Fig. 6(c). In this case ($x = 0.24$), the results in the IFE scenario are qualitatively similar to the ones already obtained for $x = 0.25$: the HD-AOS occurs with small Q with respect to the linearly polarization case for (σ^-, $m_z^{\mathrm{TM}} \uparrow$) and ($\sigma^+$, $m_z^{\mathrm{TM}} \downarrow$) [open blue symbols in Fig. 6(d)], and it requires high Q for the two other combinations [(σ^+, $m_z^{\mathrm{TM}} \uparrow$), ($\sigma^-$, $m_z^{\mathrm{TM}} \downarrow$), open red symbols in Fig. 6(d)]. However, for this concentration ($x = 0.24$), the results in the MCD scenario [see solid symbols in Fig. 6(d)] are opposite as for $x = 0.25$, and also opposite to the ones obtained in the IFE scenario.

These results can be understood as follows. In the MCD scenario, the HD-AOS depends on the net initial magnetization at room temperature ($m_N = M_s^{\mathrm{TM}} m_z^{\mathrm{TM}} + M_s^{\mathrm{RE}} m_z^{\mathrm{RE}}$, with $m_z^{\mathrm{TM}} = \pm 1$ and $m_z^{\mathrm{RE}} = \mp 1$) and on the laser helicity ($\sigma^{\pm} = \pm 1$): if initially $m_N > 0$, a laser pulse with $\sigma^+ = +1$ promotes the reversal, and this happens either for $m_z^{\mathrm{TM}} = -1$ ($m_z^{\mathrm{RE}} = +1$) when $x = 0.25$ because $M_s^{\mathrm{RE}} > M_s^{\mathrm{TM}}$ at $T = 300$ K, or for $m_z^{\mathrm{TM}} = +1$ ($m_z^{\mathrm{RE}} = -1$) if $x = 0.24$ because now $M_s^{\mathrm{TM}} > M_s^{\mathrm{RE}}$ at $T = 300$ K. On the other hand, the HD-AOS within the IFE scenario is essentially determined by the dominant sublattice magnetization just below the Curie threshold ($T \lesssim T_C$), due to the persistence of the magneto-optical field $\vec{B}_{\mathrm{MO}}(\vec{r}, t)$ when the laser pulse has already finished. Note that for both concentrations $M_s^{\mathrm{TM}} > M_s^{\mathrm{RE}}$ for $T \lesssim T_C$. Indeed, during the cooling down after the pulse, the magneto-optical field $\vec{B}_{\mathrm{MO}}(\vec{r}, t) \propto \sigma^{\pm} \vec{u}_z$ promotes *up* or *down* magnetic state for the TM for σ^+ and σ^-, respectively, and therefore, if m_z^{TM} is initially *up* ($m_z^{\mathrm{TM}} = +1$), $\vec{B}_{\mathrm{MO}}(\vec{r}, t)$ promotes the reversal for σ^- and vice. Our analysis suggests a set of experiments which could help to elucidate the physical mechanism behind these HD-AOS, just by evaluating the switching probability as function of the initial state and of the laser pulse helicity for two different concentrations x, one resulting in a TM-dominated and other in a RE-dominated FiM alloy at room temperature. Another alternative could be to use a single FiM with a given composition, and working with a cryostat to fix different initial temperatures below and above the magnetization compensation temperature. Similar results to ones obtained by changing the composition x for a fixed temperature of the thermal bath are also predicted by our simulations when it is the temperature of the thermal bath that is varied for a given composition (see Fig. S10 in Supplemental Material Note SN9 [23]): both IFE and MCD scenarios give similar results below compensation and opposite above it. These theoretical predictions on the HD-AOS could be checked by experiments, which all together would allow us to shed light on the real scope of these two mechanisms.

IV. CONCLUSIONS

As summary, the extension of the two sublattice Landau-Lifshitz-Bloch equation with the angular momentum nonequilibrium exchange is proven to be a powerful tool to study ultrafast AOS switching in ferrimagnetic alloys. The formalism here developed reproduces the atomistic spin dynamics results for small samples at the nanoscale, while it opens the possibility to numerically study realistic extended microsize systems, with dimensions comparable to the experimental ones. The deterministic single-shot switching and the demagnetization at high power regime are found to be in very good agreement with the experimental observations of helicity-independent AOS under linearly polarized laser pulses. The phase diagram combined with the thermal analysis allowed us to determine and predict the size of the inverted regions as depending the absorbed power and duration of the laser pulse. Moreover, we have also explored and reproduced experimental observations for the helicity-dependent AOS within the two physical mechanisms suggested in the literature: magnetic circular dichroism and inverse Faraday effect. According to the magnetic circular dichroism, the absorbed power by the FiM depends on the laser helicity under circularly polarized pulses, and our model also predicts the main features of the helicity-dependent AOS measurements. Indeed, both the helicity-dependent AOS and the appearance of rings around the circularly polarized laser beam appear naturally in our simulations. Additionally, similar results of the HD-AOS switching were also obtained in the inverse Faraday effect scenario, where the circular polarization has been suggested to generate a persistent magneto-optical field promoting the switching for proper combinations of initial magnetic state and laser pulse helicity. By exploring FiM samples with different compositions resulting in TM-dominated or in a RE-dominated FiM alloy at room temperature, we have found a difference between the predictions of the IFE and the MCD scenarios. These results could be tested by performing the corresponding experiments, and consequently could help together to elucidate the true basis of such HD-AOS processes. Therefore, our methods will be useful to understand recent and future experiments on AOS, and also to the develop novel recording devices where the information can be manipulated by optical means in an ultrafast fashion.

ACKNOWLEDGMENTS

This work was supported by Projects No. MAT2017-87072-C4-1-P funded by Ministerio de Educacion y Ciencia and No. PID2020117024GB-C41 funded by Ministerio de Ciencia e Innovacion, both from the Spanish government, Projects No. SA299P18 and No. SA114P20 from Consejeria de Educacion of Junta de Castilla y León, and project MagnEFi, Grant Agreement No. 860060, (H2020-MSCA-ITN-2019) funded by the European Commission. U.A. would like to acknowledge funding by the Deutsche Forschungsgemeinschaft (DFG, German Research Foundation)—Project-ID 328545488—TRR 227, Project No. A08.

[1] E. Beaurepaire, J.-C. Merle, A. Daunois, and J.-Y. Bigot, Ultrafast Spin Dynamics in Ferromagnetic Nickel, Phys. Rev. Lett. **76**, 4250 (1996).

[2] M. S. El Hadri, P. Pirro, C. H. Lambert, S. Petit-Watelot, Y. Quessab, M. Hehn, F. Montaigne, G. Malinowski, and S. Mangin, Two types of all-optical magnetization switching

mechanisms using femtosecond laser pulses, Phys. Rev. B **94**, 064412 (2016).

[3] R. Medapalli, D. Afanasiev, D. K. Kim, Y. Quessab, S. Manna, S. A. Montoya, A. Kirilyuk, T. Rasing, A. V. Kimel, and E. E. Fullerton, Multiscale dynamics of helicity-dependent all-optical magnetization reversal in ferromagnetic Co/Pt multilayers, Phys. Rev. B **96**, 224421 (2017).

[4] M. Beens, M. L. M. Lalieu, A. J. M. Deenen, R. A. Duine, and B. Koopmans, Comparing all-optical switching in synthetic-ferrimagnetic multilayers and alloys, Phys. Rev. B **100**, 220409(R) (2019).

[5] J. W. Liao, P. Vallobra, L. O'Brien, U. Atxitia, V. Raposo, D. Petit, T. Vemulkar, G. Malinowski, M. Hehn, E. Martínez, S. Mangin, and R. P. Cowburn, Controlling all-optical helicity-dependent switching in engineered rare-earth free synthetic ferrimagnets, Adv. Sci. **6**, 1901876 (2019).

[6] M. L. M. Lalieu, M. J. G. Peeters, S. R. R. Haenen, R. Lavrijsen, and B. Koopmans, Deterministic all-optical switching of synthetic ferrimagnets using single femtosecond laser pulses, Phys. Rev. B **96**, 220411(R) (2017).

[7] D. Steil, S. Alebrand, A. Hassdenteufel, M. Cinchetti, and M. Aeschlimann, All-optical magnetization recording by tailoring optical excitation parameters, Phys. Rev. B **84**, 224408 (2011).

[8] A. R. Khorsand, M. Savoini, A. Kirilyuk, A. V. Kimel, A. Tsukamoto, A. Itoh, and T. Rasing, Role of Magnetic Circular Dichroism in All-Optical Magnetic Recording, Phys. Rev. Lett. **108**, 127205 (2012).

[9] K. Vahaplar, A. M. Kalashnikova, A. V. Kimel, S. Gerlach, D. Hinzke, U. Nowak, R. Chantrell, A. Tsukamoto, A. Itoh, A. Kirilyuk, and T. Rasing, All-optical magnetization reversal by circularly polarized laser pulses: experiment and multiscale modeling, Phys. Rev. B **85**, 104402 (2012).

[10] M. O. A. Ellis, E. E. Fullerton, and R. W. Chantrell, All-optical switching in granular ferromagnets caused by magnetic circular dichroism, Sci. Rep. **6**, 30522 (2016).

[11] V. Raposo, E. Martinez, A. Hernandez, and M. Zazo, Micromagnetic modeling of all-optical switching, IEEE Trans. Magn. **55**, 1300406 (2019).

[12] A. Kirilyuk, A. V. Kimel, and T. Rasing, Ultrafast optical manipulation of magnetic order, Rev. Mod. Phys. **82**, 2731 (2010).

[13] V. Raposo, R. Guedas, F. García-Sánchez, M. A. Hernández, M. Zazo, and E. Martínez, Micromagnetic modeling of all optical switching of ferromagnetic thin films: The role of inverse faraday effect and magnetic circular dichroism, Appl. Sci. (Switzerland) **10**, 1307 (2020).

[14] A. V. Kimel, A. Kirilyuk, P. A. Usachev, R. V. Pisarev, A. M. Balbashov, and T. Rasing, Ultrafast nonthermal control of magnetization by instantaneous photomagnetic pulses, Nature (London) **435**, 655 (2005).

[15] C-H. Lambert, S. Mangin, B. S. D. Ch. S. Varaprasad, Y. K. Takahashi, M. Hehn, M. Cinchetti, G. Malinowski, K. Hono, Y. Fainman, M. Aeschlimann, and E. E. Fullerton, Ultrafast optical control of orbital and spin dynamics in a solid-state defect, Science **345**, 1337 (2014).

[16] T. A. Ostler, J. Barker, R. F. L. Evans, R. W. Chantrell, U. Atxitia, O. Chubykalo-Fesenko, S. el Moussaoui, L. le Guyader, E. Mengotti, L. J. Heyderman, F. Nolting, A. Tsukamoto, A. Itoh, D. Afanasiev, B. A. Ivanov, A. M. Kalashnikova, K. Vahaplar, J. Mentink, A. Kirilyuk, T. Rasing, and A. V. Kimel, Ultrafast heating as a sufficient stimulus for magnetization reversal in a ferrimagnet, Nat. Commun. **3**, 1666 (2012).

[17] I. Radu, K. Vahaplar, C. Stamm, T. Kachel, N. Pontius, H. A. Dürr, T. A. Ostler, J. Barker, R. F. L. Evans, R. W. Chantrell, A. Tsukamoto, A. Itoh, A. Kirilyuk, T. Rasing, and A. V. Kimel, Transient ferromagnetic-like state mediating ultrafast reversal of antiferromagnetically coupled spins, Nature (London) **472**, 205 (2011).

[18] C. S. Davies, T. Janssen, J. H. Mentink, A. Tsukamoto, A. V. Kimel, A. F. G. van der Meer, A. Stupakiewicz, and A. Kirilyuk, Pathways for Single-Shot All-Optical Switching of Magnetization in Ferrimagnets, Phys. Rev. Appl. **13**, 024064 (2020).

[19] R. Moreno, T. A. Ostler, R. W. Chantrell, and O. Chubykalo-Fesenko, Conditions for thermally induced all-optical switching in ferrimagnetic alloys: Modeling of TbCo, Phys. Rev. B **96**, 014409 (2017).

[20] P. Nieves, U. Atxitia, R. W. Chantrell, and O. Chubykalo-Fesenko, The classical two-sublattice landau-lifshitz-bloch equation for all temperatures, Low Temp. Phys. **41**, 739 (2015).

[21] C. Vogler, C. Abert, F. Bruckner, and D. Suess, Stochastic ferrimagnetic landau-lifshitz-bloch equation for finite magnetic structures, Phys. Rev. B **100**, 054401 (2019).

[22] R. F. L. Evans, W. J. Fan, P. Chureemart, T. A. Ostler, M. O. A. Ellis, and R. W. Chantrell, Atomistic spin model simulations of magnetic nanomaterials, J. Phys.: Condens. Matter **26**, 103202 (2014).

[23] See Supplemental Material at http://link.aps.org/supplemental/10.1103/PhysRevB.105.104432 for (SN1) Atomistic Spin Dynamics (ASD) model; (SN2) Micromagnetic LLB models: conventional (LLB) and extended (eLLB) cases; (SN3) Comparison between atomistic, conventional-LLB and extended-LLB models; (SN4). Phase diagram in terms of the fluence and the pulse duration; (SN5) Helicity-Dependent AOS (HD-AOS) and Magnetic Circular Dichroism (MCD); (SN6) Helicity-Dependent AOS (HD-AOS) and Inverse Faraday Effect (IFE); (SN7). Inverse Faraday Effect: magneto-optical field or induced magnetic moment; (SN8) Material inputs for two different compositions; and (SN9) Helicity-Dependent All Optical Switching: MCD and IFE for different compositions and initial temperatures.

[24] S. I. Anisimov, B. L. Kapeliovich, and T. L. Perel'man, Electron emission from metal surfaces exposed to ultrashort laser pulses, J. Exp. Theor. Phys. **39**, 375 (1974).

[25] J. Mendil, P. Nieves, O. Chubykalo-Fesenko, J. Walowski, T. Santos, S. Pisana, and M. Münzenberg, Resolving the role of femtosecond heated electrons in ultrafast spin dynamics, Sci. Rep. **4**, 3980 (2014).

[26] U. Atxitia, O. Chubykalo-Fesenko, J. Walowski, A. Mann, and M. Münzenberg, Evidence for thermal mechanisms in laser-induced femtosecond spin dynamics, Phys. Rev. B **81**, 174401 (2010).

[27] S. Gerlach, L. Oroszlany, D. Hinzke, S. Sievering, S. Wienholdt, L. Szunyogh, and U. Nowak, Modeling ultrafast all-optical switching in synthetic ferrimagnets, Phys. Rev. B **95**, 224435 (2017).

[28] C. Banerjee, N. Teichert, K. E. Siewierska, Z. Gercsi, G. Y. P. Atcheson, P. Stamenov, K. Rode, J. M. D. Coey, and J. Besbas, Single pulse all-optical toggle switching of magnetization

without gadolinium in the ferrimagnet Mn_2Ru_xGa, Nat. Commun. **11**, 4444 (2020).

[29] A. Ceballos, A. Pattabi, A. El-Ghazaly, S. Ruta, C. P. Simon, R. F. L. Evans, T. Ostler, R. W. Chantrell, E. Kennedy, M. Scott, J. Bokor, and F. Hellman, Role of element-specific damping in ultrafast, helicity-independent, all-optical switching dynamics in amorphous (Gd,Tb)Co thin films, Phys. Rev. B **103**, 024438 (2021).

[30] U. Atxitia, P. Nieves, and O. Chubykalo-Fesenko, Landau-Lifshitz-Bloch equation for ferrimagnetic materials, Phys. Rev. B **86**, 104414 (2012).

[31] J. H. Mentink, J. Hellsvik, D. v. Afanasiev, B. A. Ivanov, A. Kirilyuk, A. V. Kimel, O. Eriksson, M. I. Katsnelson, and T. Rasing, Ultrafast Spin Dynamics In Multisublattice Magnets, Phys. Rev. Lett. **108**, 057202 (2012).

[32] J. H. Mentink, Manipulating magnetism by ultrafast control of the exchange interaction, J. Phys.: Condens. Matter **29**, 453001 (2017).

[33] V. G. Bar'yakhtar, V. I. Butrim, and B. A. Ivanov, Exchange relaxation as a mechanism of the ultrafast reorientation of spins in a two-sublattice ferrimagnet, JETP Lett. **98**, 289 (2013).

[34] A. Kamra, R. E. Troncoso, W. Belzig, and A. Brataas, Gilbert damping phenomenology for two-sublattice magnets, Phys. Rev. B **98**, 184402 (2018).

[35] J. Wei, B. Zhang, M. Hehn, W. Zhang, G. Malinowski, Y. Xu, W. Zhao, and S. Mangin, All-Optical Helicity-Independent Switching State Diagram in Gd - Fe - Co Alloys, Phys. Rev. Appl. **15**, 054065 (2021).

[36] S. Wang, C. Wei, Y. Feng, Y. Cao, H. Wang, W. Cheng, C. Xie, A. Tsukamoto, A. Kirilyuk, T. Rasing, A. V. Kimel, and X. Li, All-optical helicity-dependent magnetic switching by first-order azimuthally polarized vortex beams, Appl. Phys. Lett. **113**, 171108 (2018).

[37] C. Banerjee, K. Rode, G. Atcheson, S. Lenne, P. Stamenov, J. M. D. Coey, and J. Besbas, Ultrafast Double Pulse All-Optical Reswitching of A Ferrimagnet, Phys. Rev. Lett. **126**, 177202 (2021).

[38] M. Battiato, G. Barbalinardo, and P. M. Oppeneer, Quantum theory of the inverse faraday effect, Phys. Rev. B **89**, 014413 (2014).

[39] M. Berritta, R. Mondal, K. Carva, and P. M. Oppeneer, *Ab Initio* Theory Of Coherent Laser-Induced Magnetization In Metals, Phys. Rev. Lett. **117**, 137203 (2016).